



ELSEVIER

Available online at www.sciencedirect.com

SCIENCE @ DIRECT®

Comput. Methods Appl. Mech. Engrg. 192 (2003) 3089–3107

**Computer methods
in applied
mechanics and
engineering**

www.elsevier.com/locate/cma

Strong coupling methods in multi-phase and multi-scale modeling of inelastic behavior of heterogeneous structures

Adnan Ibrahimbegović *, Damijan Markovič

Ecole Normale Supérieure de Cachan, LMT-Cachan, 61 avenue du président Wilson, 94235 Cachan Cedex, France

Received 27 February 2003; accepted 12 May 2003

Abstract

In this work we address several issues pertaining to efficiency of the computational approach geared towards modeling of inelastic behavior of a heterogeneous structure, which is represented by a multi-scale model. We elaborate in particular upon the case where the scales remain coupled throughout the computations, implying a constant communication between the finite element models employed at each scale, and only briefly comment upon our treatment of inelastic analysis of a more classical case where the scales can be separated. We also discuss different manners of representing a complex multi-phase microstructure within the framework of the finite element model constructed at that scale, selecting a model problem of two-phase material where each phase has potentially different inelastic behavior. Several numerical examples are given to further illustrate the presented theoretical considerations.

© 2003 Elsevier B.V. All rights reserved.

1. Introduction

The presently ever increasing computational resources provide an important incentive to strive for a more refined modeling of inelastic behavior of engineering structures. In that sense, the role of the traditional phenomenological models, which have been predominantly used in engineering design, is nowadays being very actively reexamined (e.g. [1]). One of the main goals of the current research in multi-scale methods for inelastic behavior is to seek a physically more sound explanation of inelastic behavior of structures, which can be provided at the scale where dissipative mechanisms would remain uncoupled and simple to interpret, which is in general referred to as the microscale. A case in point is inelastic behavior of metals, where the classical single crystal model of Taylor (e.g. see [25]) can easily be integrated within a predictive model of polycrystal plasticity used to provide the texture evolution of thin metal sheets (e.g. [18]). Unfortunately, other examples of that kind are not very numerous. In general, the interpretation of the microscale depends on the kind of material whose behavior we study; for example for granular

* Corresponding author. Tel.: +33-1-4740-2234; fax: +33-1-4740-2240.
E-mail address: ai@lmt.ens-cachan.fr (A. Ibrahimbegović).

materials the microscale can be of the grain size and thus considerably larger than plastic crystals. The representation of the microstructure depends on the kind of result we seek. For inelastic analysis and reliable prediction of the failure mechanisms, one can state that the complexity of the model which is chosen to represent the microstructure can be such that the finite element method is again the only approach which remains applicable; multi-phase material and materials with voids (e.g. [8] or [26]) are two such examples. The same complexity is also encountered at the scale characterizing the heterogeneous structure, or the so-called macroscale, requiring again the corresponding finite element model of the given structure as the only viable basis for its inelastic analysis. One thus speaks of the micro–macro finite element model.

The main interest of this work is to provide the solution strategy for such a micro–macro finite element models. Two different classes of problems in micro–macro finite element analysis can be distinguished. The first one concerns the case where the micro- and macroscales can be fully separated; the linear analysis for this kind of problems is firmly established by means of asymptotic calculus (e.g. [23] or [16]) with a number of available standard models (e.g. see [1] for a recent review). Although the direct extrapolation of those results can not be made to non-linear analysis (see [7]), one can develop a number of equivalent results for non-linear analysis both concerning the upper and lower bounds (e.g. see [2]) as well as the non-linear analysis assuming the periodicity of the microstructure (e.g. see [19] or [4]). For the problems of this kind the most important information to be obtained from the microscale and communicated upward is the inelastic dissipation (e.g. see [12]).

The second class of problems concerns the case where the scales can not be separated for either insufficient size of the total structure (e.g. see [9]) or for a complex, multi-field nature of the microstructure (e.g. [5]). The problem of this kind requires constant communication between two scales and special strategies for passing the necessary informations from one scale to another (e.g. see [15,21,28] or [6]).

In this work we examine this second class of problems of multi-scale analysis with coupled scales. In particular, we discuss how to construct the corresponding multi-scale finite element model and the solution procedure within the framework of inelastic analysis. The main contributions can be stated as follows:

- The solution method for strong coupling of two scales is proposed, which employs the implicit integration schemes at each scale requiring several iterations to converge. The ideas of the operator split method, very much similar to those used for the classical plasticity (e.g. [10]) are exploited to decide the proper order in computing iterative solutions which assures that each computed value of state variables remains admissible, thus naturally including the final, converged value.
- Three convenient finite element representations of the microstructure using structured finite element meshes in a multi-field problem are presented and compared against the exact, but inconvenient non-structured finite element mesh representation. The advantages and disadvantages of each of those representations are evaluated with respect to the chosen model problem of two-phase material, where non-linear behavior of one phase can be described by a plasticity model and the behavior of another phase is represented by a damage model.

The outline of the paper is as follows. In Section 2 we present the solution method for multi-scale finite element analysis of inelastic behavior. Three different possibilities for representing the microstructure are described in Section 3. In Section 4 we present several numerical simulations which should further illustrate the given theoretical considerations. Conclusions are drawn in Section 5.

2. Multi-scale strong coupling methods for inelastic behavior

We consider a model problem very much representative of standard three-point bending testing of inelastic behavior of a brittle structure presented in Fig. 1. When trying to interpret the test results, the need

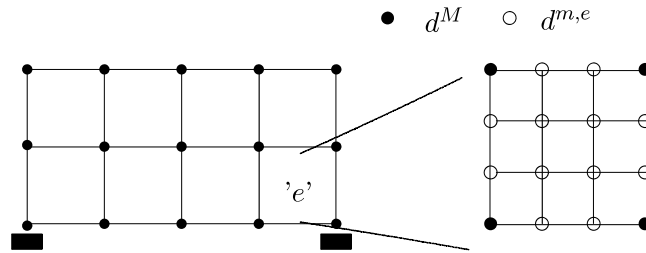


Fig. 1. Micro-macro finite element model of a simple structure.

to more easily identify the dissipative mechanisms might lead us to take into account the details of the microstructure. In other words, we would have to deal with micro-macro inelastic analysis. We do not proceed directly to treat the problem of this kind, but first recall the solution procedure for the classical plasticity constrained evolution problem, and then show that the micro-macro problem can directly benefit from such an experience.

2.1. Motivation: classical plasticity model as constrained evolution problem

We consider evolution problem in the form

$$\dot{u}(t) = Au(t); \quad u(t_n) = u_n, \quad (1)$$

for which one can provide the exact solution over given time increment with

$$u(t_{n+1}) := u_{n+1} = \exp[A\Delta t]u_n; \quad \exp[A] = \sum_{k=0}^{\infty} \frac{A^k}{k!}. \quad (2)$$

The operator split method will separate the given problem in two subproblems according to

$$A = A_1 + A_2 \Rightarrow u_{n+1} = \exp[A_1\Delta t] \exp[A_2\Delta t]u_n. \quad (3)$$

We hope to obtain a simpler problem with each of two subproblems and still be able to combine two results if the final result of one are picked up as the initial conditions for the other

$$\begin{aligned} \dot{\bar{u}} &= A_1 \bar{u} & \dot{u} &= A_2 u, \\ \bar{u}(t_n) &= u_n & u(t_n) &= \bar{u}(t_{n+1}). \end{aligned} \quad (4)$$

The obtained result, however, is only first order accurate with

$$\|\exp[A_1\Delta t] \exp[A_2\Delta t] - \exp[(A_1 + A_2)\Delta t]\| = O(\Delta t^2), \quad (5)$$

which implies that there is no point of using any higher order scheme for integrating the evolution problem. Similar conclusion can also be drawn for a non-linear evolution problem, $\dot{u} = A(u)$, see Chorin et al. [3].

One such practical example is the constrained evolution problem of the classical plasticity [24] or the generalized standard material (e.g. [20]), which can be written as the evolution equation for the state variables: displacement d (or total strain $\epsilon = \nabla^s d$), plastic strain ϵ^p and hardening variables ξ . The constrained evolution problem and its operator split representation can be written by separating elastic and plastic phase

Behavior	Elastic-fix: ϵ^p, ξ	Plastic-fix: d
$\dot{d} = K^{-1}\dot{f} \Rightarrow \dot{\epsilon} = \nabla^s d$	$\dot{\epsilon} = \nabla^s d$	$\dot{\epsilon} = 0$
$\dot{\epsilon}^p = \dot{\gamma} \frac{\partial \phi}{\partial \sigma}$	$\dot{\epsilon}^p = 0$	$\dot{\epsilon}^p = \dot{\gamma} \frac{\partial \phi}{\partial \sigma}$
$\dot{\xi} = \dot{\gamma} \frac{\partial \phi}{\partial q}$	$\dot{\xi} = 0$	$\dot{\xi} = \dot{\gamma} \frac{\partial \phi}{\partial q}$

(6)

with plastic admissibility condition

$$\dot{\gamma} \geq 0, \quad \Phi(\sigma, q) \leq 0, \quad \dot{\gamma} \Phi = 0. \quad (7)$$

One can further transform the continuum problem in (6), defined $\forall x \in \Omega$, into corresponding discrete problem by using the finite element based space discretization (e.g. [29]) and the backward Euler scheme ($\dot{\mathbf{u}} = A(\mathbf{u}) \Rightarrow u_{n+1} = u_n + \Delta t A(u_{n+1})$) to integrate the evolution equations for internal variables. Namely we can write

$$\begin{aligned} r_{n+1} &:= \sum_{e=1}^{n_{el}} [f_{n+1}^{e, \text{int}} - f_{n+1}^{e, \text{ext}}] = 0 \quad \text{in } \Omega^h, \\ f_{n+1}^{e, \text{int}} &= \int_{\Omega^e} B^{eT} \hat{\sigma}(d_{n+1}, \epsilon_{n+1}^p, \zeta_{n+1}) dx \end{aligned} \quad (8)$$

and

$$\begin{aligned} h_{n+1} &:= \begin{bmatrix} \epsilon_{n+1}^p - \epsilon_n^p - \gamma_{n+1} \frac{\partial \phi(\sigma_{n+1}, q_{n+1})}{\partial \sigma_{n+1}} \\ \zeta_{n+1} - \zeta_n - \gamma_{n+1} \frac{\partial \phi(\sigma_{n+1}, q_{n+1})}{\partial q_{n+1}} \end{bmatrix} = 0 \quad \forall \text{GNP}, \\ \gamma_{n+1} &:= \Delta t \dot{\gamma}_{n+1} \geq 0, \quad \phi(\sigma_{n+1}, q_{n+1}) \leq 0, \quad \gamma_{n+1} \phi(\sigma_{n+1}, q_{n+1}) = 0, \end{aligned} \quad (9)$$

where $A_{e=1}^{n_{el}}$ denotes the finite element assembly procedure and GNP denotes the Gaussian numerical integration points which are chosen in accordance with a selected Gaussian quadrature rule (e.g. see [29]). We note that the use of the first order time integration method, such as the backward Euler, to compute the evolution of internal variables in (9) is fully justified with respect to the maximal accuracy which one can obtain from the operator split methods. The operator split method applied to the discrete problem will separate the solution of the global set of equilibrium equations in (8) from the local equations in (9), with each one pertaining only to one Gauss quadrature point. The solution is constructed according to the following iterative strategy: one global iteration is followed by, in general, several local iterations, which should allow the convergence of the local equation in (9) for each iterative value of global variable. If (i) and (j) are, respectively, the counters of the global and local iterations, one can write

FOR (i) = 1, 2, ...

$$K_{n+1}^{(i)} \Big|_{\epsilon_{n+1}^p, \bar{\zeta}_{n+1}, \bar{\gamma}_{n+1}} \left(d_{n+1}^{(i+1)} - d_{n+1}^{(i)} \right) = -r_{n+1}^{(i)} \Big|_{\epsilon_{n+1}^p, \bar{\zeta}_{n+1}, \bar{\gamma}_{n+1}} \quad (10)$$

FOR (j) = 1, 2, ...

$$\frac{\partial h_{n+1}^{(j)}}{\partial \tilde{\mathbf{u}}_{n+1}} \Big|_{d_{n+1}^{(i)}} \left(\tilde{\mathbf{u}}_{n+1}^{(j+1)} - \tilde{\mathbf{u}}_{n+1}^{(j)} \right) = -h_{n+1}^{(j)} \Big|_{d_{n+1}^{(i)}}; \quad \tilde{\mathbf{u}} = [\epsilon^p, \zeta, \gamma] \quad (11)$$

IF $\|h_{n+1}(d^{(i)}, \epsilon^{p(j+1)}, \zeta^{(j+1)}, \gamma^{(j+1)})\| \leq \text{tol.} \Rightarrow (i) \leftarrow (i+1)$

ELSE (j) $\leftarrow (j+1)$

Both iteration loops are carried out until convergence, which leads to the strong coupling solution procedure which is unconditionally stable [17]. We note that the converged result in local iteration in (11) will furnish plastically admissible stress state σ_{n+1} which satisfies the yield criterion $\Phi(\sigma_{n+1}) \leq 0$; see Fig. 2 for illustration.

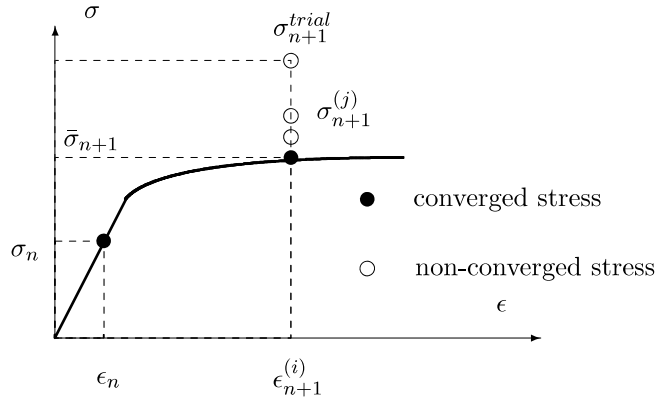


Fig. 2. Local computation of plastically admissible stress state.

2.2. Multi-scale non-linear analysis with strong coupling of scales

Having reviewed the pertinent details from the classical plasticity problem, in this section we set to show that quite an equivalent problem is found in multi-scale analysis for the case where the scales remain strongly coupled imposing the constant communication between the scales. More precisely, we deal with the analysis of the non-linear behavior of a heterogeneous structure, where one is obliged to go down to microscale to more easily identify a particular failure mechanism. This scale can be as small as 1 μm for metals or as large as 1 cm for concrete, so that “microscale” should be interpreted in the relative sense as being much smaller than the macroscale characterizing the structural dimension, with the order of 1 cm for metals or as much as 1 m for concrete.

Two-scale finite element model can then be constructed for such a structure as shown in Fig. 1, where the finite element representation is provided for each scale. Without loss of generality we assume that all the internal variables are defined only at the microscale, which implies that the state variables can be written as: displacements at the macroscale, d_{n+1}^M , displacements at the microscale, d_{n+1}^m and the internal variables governing the evolution of inelastic dissipation at the microscale, $\omega_{n+1}^{m,e}$. We note that subscript “ $n+1$ ” indicates that we refer to the state variables at the time t_{n+1} in the discrete model. This can be presented more formally in terms of

Central problem: Micro–macro inelastic analysis for a typical time step $\Delta t = t_{n+1} - t_n$

Given: $d_n^M, d_n^{m,e}, \omega_n^e; \forall e \in [1, n_{cl}^M]$

Find: $d_{n+1}^M, d_{n+1}^{m,e}, \omega_{n+1}^e$

Such that the equilibrium at macroscale and those at each microscale are all satisfied

$$r_{n+1} := \left. \sum_{e=1}^{n_{cl}^M} (f_{n+1}^{M,e,int} - f_{n+1}^{e,ext}) \right|_{d^{m,e}} = 0 \mapsto d_{n+1}^M \mapsto d_{n+1}^{M,e} = L^e d_{n+1}^M \quad (12)$$

$$h_{n+1}(d_{n+1}^{m,e}, \omega_{n+1}^e)|_{d^{m,e}} = 0; \quad \forall e \in [1, n_{cl}^M] \quad (13)$$

where L^e denotes the Boolean connectivity matrix. The structure of the micro–macro equilibrium equation is very much similar to those in (8) and (9) for the classical plasticity model in the sense that the first part in

(12) are global equations which concern the macroscale, whereas the second part in (13) are local equations which concern one microstructure at the time. This analogy allows us to directly use the operator split method in order to separate the global from local equations solving. In other words, for each one of global iterations (i), we carry out in general several local iterations (j) which should lead to converged solutions of (13). First, in each global iteration at the macroscale one solves the linearized form of the structure equilibrium equations with

FOR (i) = 1, 2, ...

$$\text{Lin}[r_{n+1}] = 0 \Rightarrow \underbrace{\text{"}K_{n+1}^{(i)}\text{"}}_{?} \left(d_{n+1}^{M,(i+1)} - d_{n+1}^{M,(i)} \right) = f_{n+1}^{\text{ext}} - \underbrace{\text{"}f_{n+1}^{\text{int},(i)}\text{"}}_{?}, \quad (14)$$

where macroscale stiffness and internal force vector are obtained by the finite element assembly-like procedure taking into account the corresponding converged values at the microscale. In other words, we can write

$$\text{"}f_{n+1}^{\text{int},(i)}\text{"} := \sum_{e=1}^{n_{\text{el}}^M} L^{e,T} f_{n+1}^{M,e,\text{int},(i)} \bigg|_{d^{m,e}, \omega^e} \quad (15)$$

and

$$\text{"}K_{n+1}^{(i)}\text{"} := \sum_{e=1}^{n_{\text{el}}^M} L^{e,T} K_{n+1}^{M,e,\text{int},(i)} \bigg|_{d^{m,e}, \omega^e} L^e, \quad (16)$$

where we denoted by L^e , the Boolean connectivity matrix which identifies the displacement vector components which are of interest for a particular microstructure (see also (12)).

The latter is a part of a more general procedure, usually referred to as localization, where one recovers all the displacement components at the microscale which are directly constrained to the macroscale displacements. To fix these ideas, one can introduce the transformation matrix T^e for each microstructure to obtain all the values of the constrained microstructure displacements

$$\bar{d}_{n+1}^{m,e,(i)} = T^e d_{n+1}^{M,e,(i)}. \quad (17)$$

For instance, the simplest possibility is to choose T^e to be the linear interpolation between two adjacent macromesh nodes (see Fig. 3).

The local iteration can then be started. At first iteration, one simply applies the imposed microscale displacement field according to (see [13])

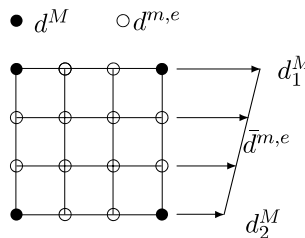


Fig. 3. Choice of the localization matrix T^e from the linear interpolation of the micronodes displacements $\bar{d}^{m,e}$ between two adjacent macronodes displacements $d_{1,2}^M$.

$$\text{Lin}[h_{n+1}^e] = 0 \Rightarrow \bigwedge_{e=1}^{n_{\text{el}}^{m,e}} \left[K_{n+1}^{m,e,(1)} (d_{n+1}^{m,e,(1)} - d_n^{m,e}) = \overbrace{-h_n^e}^{=0} - \bar{K}_{n+1}^{m,e} (\bar{d}_{n+1}^{m,e,(i)} - \bar{d}_n^{m,e}) \right], \quad (18)$$

where $K_{n+1}^{m,e,(1)}$ are the finite element stiffness matrices obtained from the finite element model of the microstructure for active nodes, whereas $\bar{K}_{n+1}^{m,e}$ are the stiffness matrices which pertain to the constrained microscale nodes.

The subsequent local iterations are then carried out with the update of internal variables and microscale displacements

FOR $(j) = 1, 2, \dots$

$$\omega_{n+1}^{m,e,(j+1)} \leftarrow \omega_n^{m,e,(j)} + \Delta \omega_n^{m,e,(j+1)} \quad (19)$$

$$\text{Lin}[h_{n+1}^{e,(j)}] = 0 \Rightarrow \bigwedge_{e=1}^{n_{\text{el}}^{m,e}} \left[K_{n+1}^{m,e,(j)} (d_{n+1}^{m,e,(j+1)} - d_n^{m,e,(j)}) = -h_{n+1}^{e,(j)} \right] \quad (20)$$

IF $\|h_{n+1}^{e,(j+1)}\| > \text{tol.}(j) \leftarrow (j+1)$

until the final convergence is achieved to obtain

ELSE $\|h_{n+1}^{e,(j+1)}\| \leq \text{tol}$ finish local iterations

$$\text{Lin}[h_{n+1}^{e,(j+1)}] = 0 \Rightarrow \begin{bmatrix} K_{n+1}^{m,e} & \bar{K}_{n+1}^{m,e} \\ \bar{K}_{n+1}^{m,e,T} & \bar{\bar{K}}_{n+1}^{m,e} \end{bmatrix} \begin{bmatrix} d_{n+1}^{m,e,(j+1)} - d_n^{m,e} \\ \bar{d}_{n+1}^{m,e} - \bar{d}_n^{m,e} \end{bmatrix} = \begin{bmatrix} \overbrace{-h_{n+1}^{e,(j+1)}}^{=0} \\ -\bar{h}_{n+1}^{m,e} \end{bmatrix}. \quad (21)$$

The static condensation of Wilson [27] can then be applied to set of equations in (21) to obtain

$$\underbrace{\left[\bar{\bar{K}}_{n+1}^{m,e} - \bar{K}_{n+1}^{m,e,T} [K_{n+1}^{m,e}]^{-1} \bar{K}_{n+1}^{m,e} \right]}_{\hat{K}_{n+1}^{m,e}} (\bar{d}_{n+1}^{m,e,(i)} - \bar{d}_n^{m,e}) = \underbrace{-\bar{h}_{n+1}^{m,e} + \bar{K}_{n+1}^{m,e,T} [K_{n+1}^{m,e}]^{-1} \overbrace{h_{n+1}^{e,(j+1)}}^{=0}}_{\hat{f}_{n+1}^{m,e}}. \quad (22)$$

The last phase of the local solution procedure is to perform homogenization in order to transform the pertinent information to macroscale and in particular provide the microscale stiffness and residual vector for computing the results in (15) and (16). One can thus make use again of the transformation matrix to write

$$\begin{aligned} f_{n+1}^{M,e,\text{int},(i)} &= T^{e,T} \hat{f}_{n+1}^{m,e}, \\ K_{n+1}^{M,e,\text{int},(i)} &= T^{e,T} \hat{K}_{n+1}^{m,e} T^e \end{aligned} \quad (23)$$

for the elementary contributions to the internal force vector and the structure stiffness matrix to be assembled in (15) and (16), respectively.

3. Microstructure representation for multi-phase materials

The computational framework presented in the previous section relies on the finite element representation of the microstructure in order to explain the failure mechanism. Among a very large number of

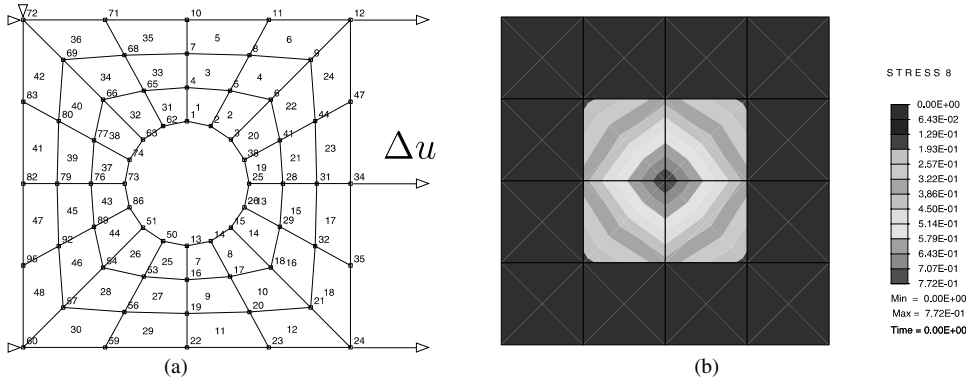


Fig. 4. Finite element representations of the two-phase material microstructure: (a) exact mesh, where the elements conform with the microstructure (b) structured mesh, where the mesh is regular and there occur heterogeneities within the elements. The contour in (b) presents the value of the characteristic function $\kappa(x) = 0$ if $x \in \Omega_{\text{matrix}}$ and $\kappa(x) = 1$ if $x \in \Omega_{\text{void}}$, where Ω_{matrix} and Ω_{void} denote the structural matrix and void volume part, respectively.

different possibilities we chose herein a model problem of two-phase material where the inelastic behavior of one phase can be described by a plasticity model and the inelastic behavior of the other phase can be represented by a damage model. One can find a number of real materials whose inelastic behavior can be described by a two-phase model of this kind, from the porous metals with damage phase with a vanishing value of damage stress representing the voids, to concrete material where the cement paste behavior is described by a plasticity model and the aggregate behavior is described by a damage model.

Moreover, for the chosen model problem we select a simple microstructure shown in Fig. 4, where the damage phase occupies a region of circular shape surrounded by the plastic phase spreading to the boundaries of the square cell corresponding to the representative volume element. We will consider three different convenient representations of such a microstructure constructed by using the structured finite element mesh: (i) Gaussian numerical point (GNP) filtering, (ii) smeared stress representation and (iii) incompatible mode representation.

The accuracy of these representations is compared against the microstructure representation, which is referred to as “exact”, in the sense that the finite element mesh is exactly adjusted to the domains occupied by each phase, so that every finite element corresponds to a subdomain occupied by only one phase. On the other hand, all three structured representations of the microstructure are only approximate, in that each finite element is of a rectangular shape and the same size, and therefore one element domain can be shared between both phases.

The first structured representation, referred herein as the GNP filtering, is a simple idea (e.g. [28]) where the properties used for the computation of element arrays by using Gaussian numerical integration correspond to either one phase or another, depending upon where the particular Gauss point is located, namely within the plastic phase or within the damage phase.

The second representation by the smeared stress model is also an approximate representation of the microstructure where within the structured mesh of the representative volume element each finite element is given the same material properties corresponding to a smeared model where two-phase behavior is represented by a coupled plasticity-damage model. The latter is obtained by the homogenization procedure (see [11]) which is carried out as follows. For the imposed total strain field at the level of the representative volume element we will assume that the additive decomposition will apply

$$\epsilon = \epsilon^e + \epsilon^p + \epsilon^d, \quad (24)$$

separating the total strain into elastic, ϵ^e , plastic, ϵ^p , and damage strain component, ϵ^d . The elastic domain for the model problem is defined by the combination of the yield and damage criteria, each one with no hardening effect

$$\Phi^p(\sigma) = \|\text{dev}(\sigma)\| - \sqrt{\frac{2}{3}}\sigma_y \leq 0, \quad (25)$$

$$\Phi^d(\sigma) = \text{tr}(\sigma) - \sigma_f \leq 0. \quad (26)$$

It follows from (25), (26) that two failure mechanisms, the shear stress yielding and damage under hydrostatic stress state, are both represented in the model. The final ingredient of the model is the strain energy given as

$$\Psi(\epsilon, \epsilon^p, \epsilon^d, D) = \underbrace{\frac{1}{2}\epsilon^e C \epsilon^e}_{\Psi^e(\epsilon^e)} + \underbrace{\sigma \epsilon^d - \frac{1}{2}\sigma D \sigma}_{\Psi^d(\epsilon^d, D)}, \quad (27)$$

where C is the elastic modulus and D is the damage compliance. All remaining ingredients can be obtained (see [11]) from the standard thermodynamic considerations of the second principle and the maximum of inelastic dissipation principle. In particular one computes initially the stress by either plasticity or damage model component, and then seeks to pick the damage strain so that either computed stress will finally have the same value, and moreover will adhere to the admissible elastic domain

$$\left. \begin{aligned} \sigma_{n+1} &:= C(\epsilon_{n+1} - \epsilon_{n+1}^p - \epsilon_{n+1}^d) = D_{n+1}^{-1} \epsilon_{n+1}^d \\ \gamma_{n+1}^p \Phi^p(\sigma_{n+1}) &= 0; \quad \gamma_{n+1}^d \Phi^d(\sigma_{n+1}) = 0 \end{aligned} \right\} \Rightarrow \epsilon_{n+1}^d. \quad (28)$$

The third structured finite element representation employs the incompatible mode 4-node element (see [14]) in order to provide a satisfying microstructure representation within each rectangular element. For a typical element with the domain shared between two phases, the equilibrium and compatibility conditions along the phase interface can be exploited to deduce the admissible values of stress and strains. More precisely, for the phase interface orientation specified by the unit normal vector n (or the unit tangent vector m , such that $m \cdot n = 0$ and $\|n\| = \|m\| = 1$) the traction equilibrium and the Cauchy principle imply that

$$t_n^+ = t_n^- \Rightarrow \begin{cases} \sigma_{nn}^+ = \sigma_{nn}^- \Rightarrow \epsilon_{nn}^+ \neq \epsilon_{nn}^-, \\ \sigma_{nm}^+ = \sigma_{nm}^- \Rightarrow \epsilon_{nm}^+ \neq \epsilon_{nm}^-, \end{cases} \quad (29)$$

whereas the compatibility for the perfect interface bond should lead to

$$\epsilon_{mm}^+ = \epsilon_{mm}^- \Rightarrow \sigma_{mm}^+ \neq \sigma_{mm}^-, \quad (30)$$

with $(\cdot)^+$ and $(\cdot)^-$ indicating the values at the opposite sides of the phase interface. It thus follows that the strain jump at the interface can be expressed according to

$$[[\nabla u]] = g \otimes n, \quad g = \alpha n + \beta m \Rightarrow [[\epsilon]] = \alpha n \otimes n + \beta \text{sym}(m \otimes n). \quad (31)$$

In the finite element implementation these strain jumps are introduced in terms of incompatible modes (e.g. see [14]), superposed upon the standard interpolation of a 4-node element (Fig. 5) which results with (e.g. see [22])

$$u \approx \sum_{a=1}^4 N_a d_a + \alpha \hat{n} + \beta \hat{m}, \quad (32)$$

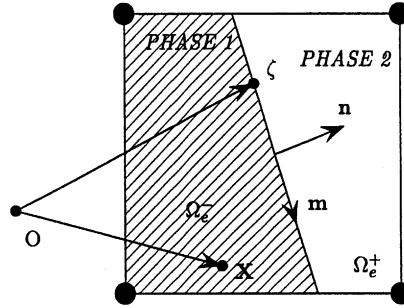


Fig. 5. The boundary between two phases intersecting an element of the structured mesh of the incompatible mode microstructure representation (see Eqs. (33) and (34)).

where

$$\hat{n}_i(x) = \begin{cases} \theta n_i [n \cdot (x - \zeta)]; & n \cdot (x - \zeta) \geq 0, \\ (1 - \theta) n_i [n \cdot (x - \zeta)]; & n \cdot (x - \zeta) < 0, \end{cases} \quad (33)$$

$$\hat{m}_i(x) = \begin{cases} \theta m_i [n \cdot (x - \zeta)]; & n \cdot (x - \zeta) \geq 0, \\ (1 - \theta) m_i [n \cdot (x - \zeta)]; & n \cdot (x - \zeta) < 0, \end{cases} \quad (34)$$

ζ being the position vector of a point on the material discontinuity and θ a parameter to determine. The corresponding deformation field is calculated as the symmetric part of the displacement gradient

$$\epsilon(x) = \nabla^S u(x) \approx \sum_{a=1}^4 B_a(x) d_a + \tilde{\epsilon}, \quad (35)$$

where

$$\tilde{\epsilon}(x) = \alpha \begin{cases} \theta n \otimes n; & n \cdot (x - \zeta) \geq 0, \\ (1 - \theta) n \otimes n; & n \cdot (x - \zeta) < 0, \end{cases} \quad (36)$$

$$+ \frac{1}{2} \beta \begin{cases} \theta (n \otimes m + m \otimes n); & n \cdot (x - \zeta) \geq 0, \\ (1 - \theta) (n \otimes m + m \otimes n); & n \cdot (x - \zeta) < 0. \end{cases} \quad (37)$$

The parameter θ is chosen to assure the patch test (e.g. see [29]) satisfaction according to

$$\int_{\Omega_e} \tilde{\epsilon} d\Omega = 0 \Rightarrow \theta = \frac{\Omega_e^-}{\Omega_e}; \quad \Omega_e = \Omega_e^+ + \Omega_e^-, \quad (38)$$

where Ω_e is the total volume of the element and Ω_e^- the part of the element volume on the “negative” side of the phase interface (shaded area on Fig. 5). Any element crossed by the phase interface is further processed in the standard manner for the incompatible mode method [14].

The issues of accuracy and efficiency of different structured mesh microstructure representations are examined in the next section in application to several numerical examples.

4. Numerical simulations

In this section we provide the results of several numerical simulations, which should confirm and further illustrate the given theoretical considerations. All computations are carried out by a research version of the computer program *FEAP*, written by Prof. Taylor at UC Berkeley (e.g. see [29]).

4.1. Numerical simulations with porous material

4.1.1. Three-point bending test

The first example concerns the three-point bending test simulation, where one considers a simple beam of span l supported at the corners (fixing all the nodes over $l/16$) and loaded in the middle by a vertical loading, which is spread over $l/8$. The beam is supposed to be built of macroelements shown in Fig. 4, where the circular central region corresponds to a void. The remaining space is filled with a matrix of either elastic or elasto-plastic material. The chosen elastic properties are: the bulk modulus $K = 2.00 \times 10^5$ MPa and the shear modulus $G = 0.92 \times 10^5$ MPa, whereas the plasticity model considers the saturation hardening of exponential type with $q^p = (\sigma_\infty - \sigma_y)(1 - \exp(-\beta \xi^p))$, where $\sigma_\infty = 5.00 \times 10^3$ MPa, $\sigma_y = 2.5 \times 10^3$ MPa and $\beta = 150$.

The first part of analysis is performed for the linear elastic behavior of the matrix. We focus mainly upon the convergence properties of the structural model for different number of subdivisions in each macroelement as well as for two different scale transition rules: the first considering only displacement interpolations and the second considering both the displacement and stress interpolations between micro- and macro-scales. The latter corresponds directly to the well known Pian-Sumihara mixed element (e.g. see [29]), where displacement interpolations are globally continuous whereas the stress interpolation is continuous within the elements, but discontinuous between the elements.

The results obtained for the internal energy of the structure, $E^e = (1/2)\epsilon C \epsilon$, obtained for different FE meshes for increasing number of macroelements are presented in Fig. 6. We can see from Fig. 6 that higher subdivisions lead to increased rate of convergence, especially for a coarse mesh. We can also see that the transition between the scales which concerns both the displacement and stress interpolations lead to even more improved results for coarse meshes. On the other hand, once the mesh is sufficiently refined all the models give the same (converged) results.

The same kind of global convergence for the refined mesh is obtained for the inelastic behavior of the matrix, for 1×1 and 2×2 displacement transition subdivisions. Namely, we have shown in Figs. 7 and 8 the convergence of the results computed for the elastic energy

$$E^e = \frac{1}{2} \int_{\Omega} \epsilon_{ij}^e C_{ijkl} \epsilon_{kl}^e d\Omega \quad (39)$$

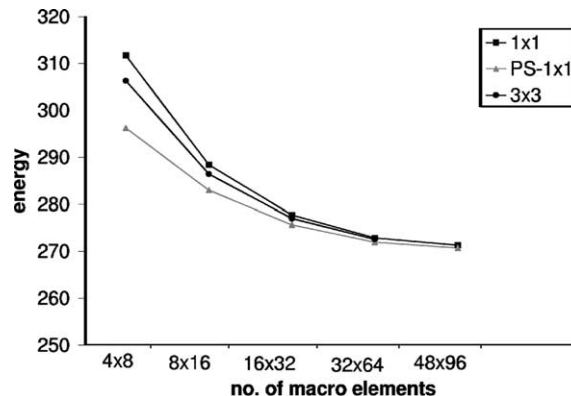


Fig. 6. Convergence of internal energy with increasing number of macroelements for displacement transition with 1×1 and 3×3 subdivisions of each macroelement and both displacement and stress transition (Pian-Sumihara element).

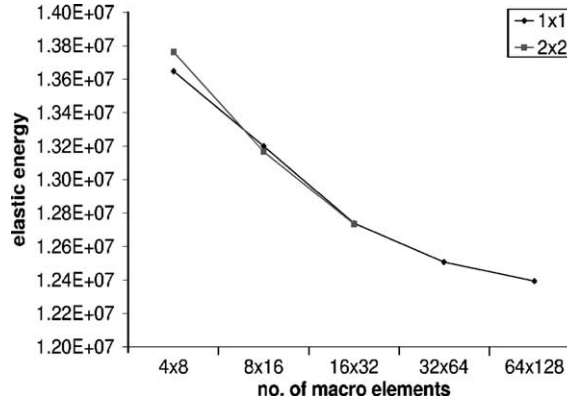


Fig. 7. Total elastic energy (Eq. (39)) for displacement transition subdivisions 1×1 and 2×2 .

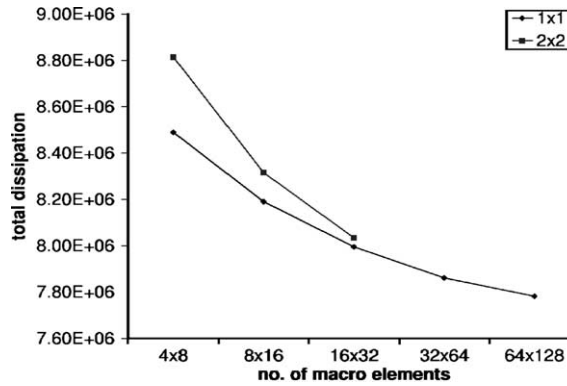


Fig. 8. Total dissipation (Eq. (40)) for displacement transition subdivisions 1×1 and 2×2 .

and the total (plastic) dissipation

$$\mathcal{D}^p = \int_{t_1}^{t_2} \int_{\Omega} (\sigma_{ij} \dot{\epsilon}_{ij}^p + q^p \dot{\xi}^p) d\Omega dt \quad (40)$$

with respect to the increasing number of macroelements.

In the contrast to the linear analysis (Fig. 6) the Figs. 7 and 8 show that the subdivided elements do not necessarily give much better results in inelastic analysis than the simple macroscopic elements. If the convergence of the elastic energy is hardly better, the subdivision 2×2 does not improve the convergence of the dissipation at all. It is however surprising that adding the degrees of freedom by subdividing the macroelement into several microelements gives worse results in respect of the total dissipation value. We assume that the localization transformation, taken simply as the linear interpolation of the micronode displacements between two adjacent macronodes (see Eq. (17) and Fig. 3), is less exact for the refined (subdivision) calculations in the cases when the fields u , ϵ , σ are more heterogeneous, that is, for the elastoplastic material analysis. The same example was used to check the quadratic convergence rates of the global solution scheme which is shown in Table 1.

4.1.2. Microstructure representation of porous materials

The second part of the study of the porous materials concerns the possible microstructure representation and the resulting failure mechanism. For this part of the analysis the hardening is suppressed and the matrix

Table 1

Global and local convergence rates for micro–macro elasto-plastic analysis of the three-point bending test

Macro iter.	Macro resid. energy	Micro iter.	Micro resid. energy
1	1.96×10^6	1	4.34×10^4
		2	6.70×10^0
		3	3.16×10^{-7}
		4	8.19×10^{-22}
2	2.11×10^4	1	1.55×10^6
		2	2.30×10^0
		3	7.53×10^{-3}
		4	1.86×10^{-14}
3	8.61×10^0	1	9.34×10^3
		2	2.61×10^{-3}
		3	6.94×10^{-14}
4	7.75×10^{-6}	1	6.06×10^0
		2	1.93×10^{-10}
5	7.45×10^{-17}	1	6.22×10^{-3}
		2	2.80×10^{-6}
		3	5.54×10^{-20}

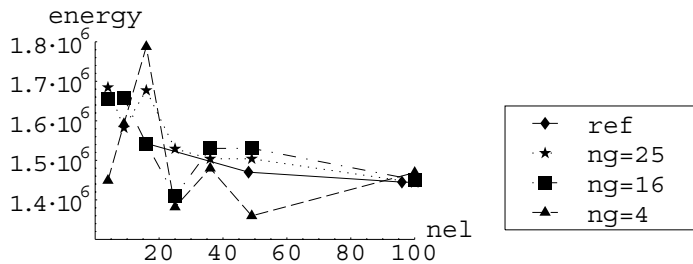


Fig. 9. Energy dependance (Eq. (39)) on the number of elements in the mesh for the linear analysis for different Gaussian quadrature schemes, 2×2 , 4×4 and 5×5 . The “ref” denotes the reference value of the analysis with the exact FE microstructure representation.

is assumed to be elastic–perfectly plastic. The reference result for the response of a single macroelement in a simple tension test is obtained by the exact finite element representation of the microstructure with the finite element mesh limited to the region occupied by the matrix. The other numerical results shown in Fig. 9 are obtained for the structured finite element mesh representation of a single macroelement where each microelement is of the same size and same square shape (see Fig. 4).

The material properties of each microelement are evaluated only at the chosen Gauss quadrature points and taken to correspond to elastic–perfectly plastic behavior if they belong to the region occupied by matrix or to a damage model with very small value of fracture stress, which can be considered as a regularized, penalty-like representation of the void chosen to avoid the singularity of the stiffness matrix of the macroelement. We can see from Fig. 9 that higher order integration rules are needed in order to represent heterogeneous properties of a single microelement, but that all different choices of Gauss quadrature rule will lead to the same result if the mesh is sufficiently refined.

However, the convergence of this kind of quadrature result stands in sharp contrast with the difficulties one is likely to experience with more local-type informations, such as failure modes. Namely, in Fig. 10 we can see that the true failure mode obtained by the exact representation of the microstructure, leading to

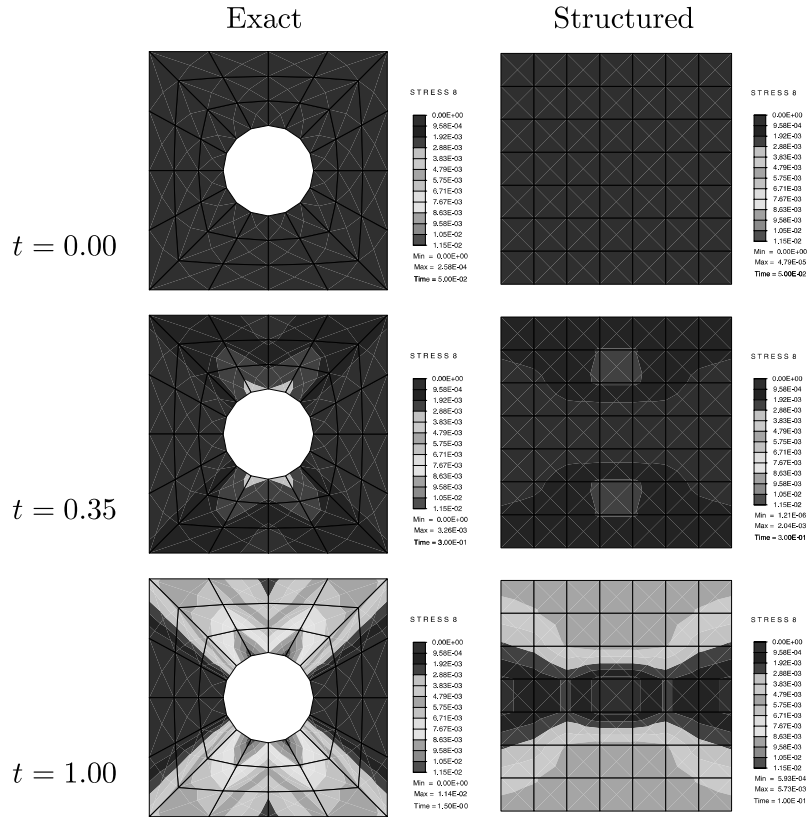


Fig. 10. Failure mechanisms of two-phase microstructure with the exact FE and structured microstructure representation.

shear band patterns, cannot be reproduced in a satisfying manner by the structured mesh, which is capable of giving only an inaccurate smeared representation.

4.2. Numerical simulations with two-phase material

In the second example we study inelastic behavior of a two-phase material composed of the matrix with elastic–perfectly plastic behavior and the circular shape fibers whose behavior can be described by the damage model with no hardening. The radius of the fibers is chosen so that the phases have equal volume fraction, 50%. The elastic properties of the matrix and the fiber are taken to be the same, with the bulk modulus $K = 77.9 \times 10^3$ MPa and the shear modulus $G = 24.9 \times 10^3$ MPa; the yield stress in the matrix is $\sigma_y = 40$ MPa, the fracture stress of the fiber is $\sigma_f = 40$ MPa and the coefficient indicating the participation of deviatoric stress in damage criterion $\alpha = 0.01$, i.e. instead of the form of Φ^d in (26) we take

$$\Phi^d = \alpha \|\text{dev}(\sigma)\|^2 + (1 - \alpha) \text{tr}^2(\sigma) - \sigma_f. \quad (41)$$

The correction of the damage surface is needed to more easily compare the three different microstructure representations. Namely, it turns out that the FE analysis based on the integration point filtering microstructure representation (see Fig. 4) does not give sensible results if we take $\alpha = 0.0$. In this particular case the matrix can only be submitted to the deviatoric part of the plastic deformation and the inclusion phase can only damage so that the spherical part of the inelastic deformation is non-zero. So, by taking the

standard $Q4$ isoparametric element interpolation, identical in both phases, we encounter a sort of inelastic deformation locking if the plastic or damage deformations become significant. The presence of phases with decoupled non-linear behavior causes non-physical elastic deformations and thus stiffer material response. The feature is depicted in the simple tension test in the next subsection.

4.2.1. Simple tension test

To compare the three different microstructure representations, exact FE, integration point filtering and smeared representation, we carry out the numerical simple tension test on the specimen shown in Fig. 11, consisting of the elasto-plastic metal matrix and 6×3 damage inclusions. The value of the applied displacement is $\Delta u = 0.02l$, l being the span of the specimen.

First we compare the analyses using the integration filtering microstructure representation for different values of the damage surface parameter α (see Eq. (41)). The comparison is made upon the force–displacement diagram (Fig. 12), taking the x components of the two. For $\alpha = 0$, we clearly observe the monotonous increasing value of the force as the function of the displacement in spite of saturating stress material constitutive laws for either phase. For $\alpha > 0.0$ the force saturates as expected.

In Fig. 13 we compare the three structured representations of the microstructure for the case where the parameter of the damage phase model is $\alpha = 0.01$. The reference value is obtained by the exact FE representation, which should give the best approximation at the price of more degrees of freedom and an increase in computation time. For each of those cases in Fig. 13 we can distinguish three phases of the force–displacement trajectory: elastic, hardening and saturated phase. Note that the hardening is a structural effect, since neither matrix nor inclusions can harden. We note that the integration point filtering

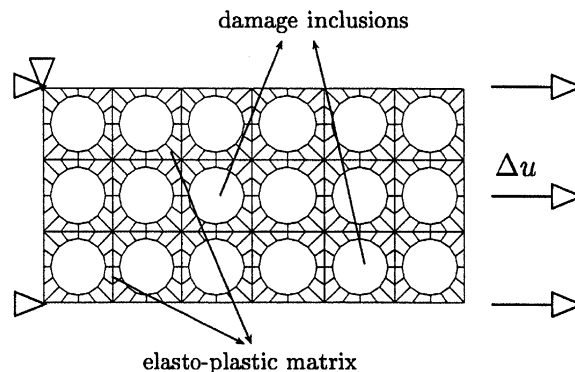


Fig. 11. Simple tension test on the heterogeneous specimen with an elasto-plastic and a damage phase.

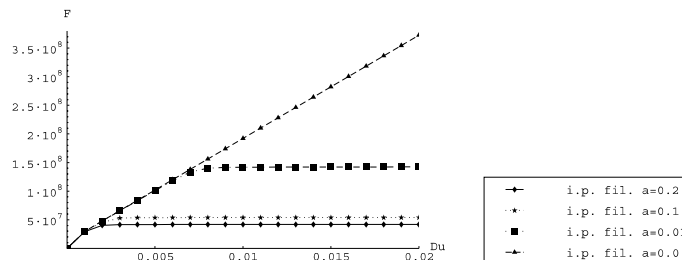


Fig. 12. Force displacement graph of the integration point filtering microstructure representation for different damage surfaces ($\alpha = 0.2, 0.1, 0.01$ and 0.0 , see Eq. (41)).

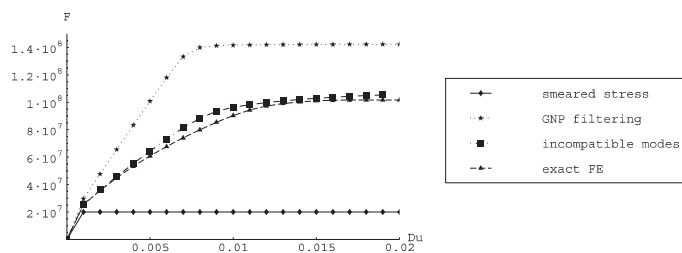


Fig. 13. Force–displacement diagrams obtained by different microstructure representations in the simple tension test of the specimen shown in Fig. 11.

representation leads to much stiffer hardening phase and higher saturated force. The latter is, however, attained sooner than for the exact FE representation. On the other hand, the smeared stress model gives significantly softer results and skips completely the hardening phase of the evolution. The fact that the smeared stress approach gives lower stresses is not very surprising. Namely, in its formulation we suppose that the stresses of the matrix and inclusion phase are the same in every integration point, whereas it is known from the homogenization theory (e.g. [1]) that the assumption of homogeneous stresses leads to the lower (Reuss) bound of the material stiffness. Finally, the incompatible mode representation provides the best results of capturing global force–displacement response. Namely, without the inconvenience of the exact FE representation we get practically the same quality of the results.

So far we have compared the macroscopic behavior of the structure, described by different microstructure representations, but we may also be interested in the microstructure evolution within the specimen. In Fig. 14 we compare the stress fields through two scalar values $|\text{dev}(\sigma)|$ and $\text{tr}(\sigma)$ for the exact FE and integration point filtering representation. For the smeared model, the deformation and stress fields are homogeneous and we have no microstructural information. As expected from the force–displacement diagram (see Fig. 13) the integration point filtering representation leads to bigger average stresses, which we can observe from Fig. 14. Nevertheless, it does not reproduce the stress peaks and localization of stresses as the exact FE representation does.

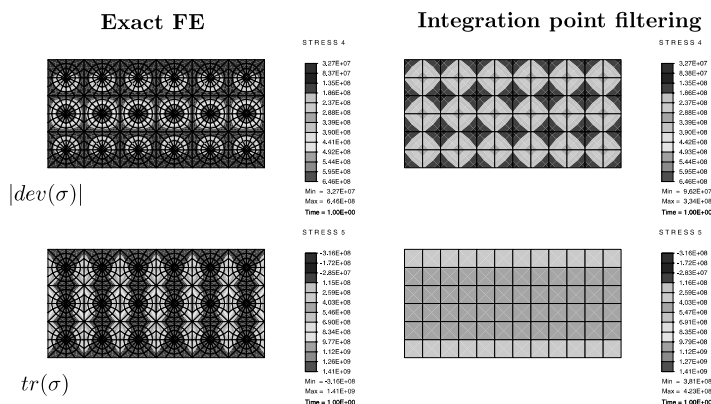


Fig. 14. Contour plots of deviatoric part, $|\text{dev}(\sigma)|$, and spherical part of the stress tensor for exact and integration point filtering representation.

4.2.2. Three-point bending test

We do the same kind of numerical three-point bending test as for the case of porous materials. The specimen, which consists of the same composite material as the one of the simple tension test, is shown in the Fig. 15, including the applied boundary conditions. The actual calculations take advantage of the symmetry and are carried out on the half of the structure only.

As in previous subsection we compare the different microstructure representations on the basis of the force–displacement curves. We impose the displacements values in the central section (Fig. 15) and identify the force as the sum of all the reactions at the corresponding nodes.

In the Fig. 16 we see similar tendencies of the force–displacement curves as in the Fig. 13 for the simple tension test. Namely, we also note the three phases of the evolution: elastic, hardening and saturation phase, but in this case the hardening phase is much less significant. Hence, the smeared model gives better results in respect of the simple tension test, since it is completely incapable to reproduce the hardening phase. On the other hand, GNP filtering agrees even less with the exact FE curve. Finally, although the agreement of the incompatible mode representation is less remarkable than for the simple tension test, it is still the most precise.

From the results in Figs. 13 and 16 we conclude that for the three-point bending test the solution corresponds better to the homogeneous stress condition, while the simple tension test solution corresponds more to the homogeneous deformation condition. Consequently, the GNP filtering approach works better for the simple tension test and the smeared stress model is more adequate for the three-point bending test.

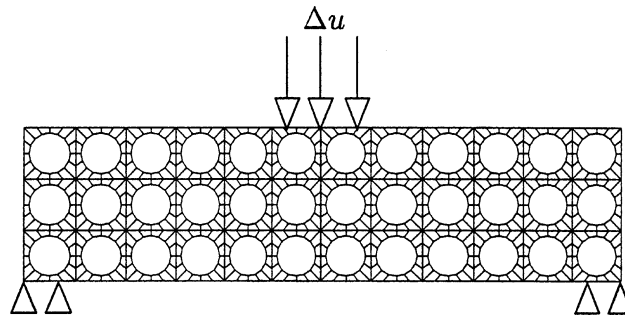


Fig. 15. Three-point bending test on the heterogeneous specimen. The displacements, $\Delta u = -0.04$, in y direction are applied on the central part of length $(1/8)l$.

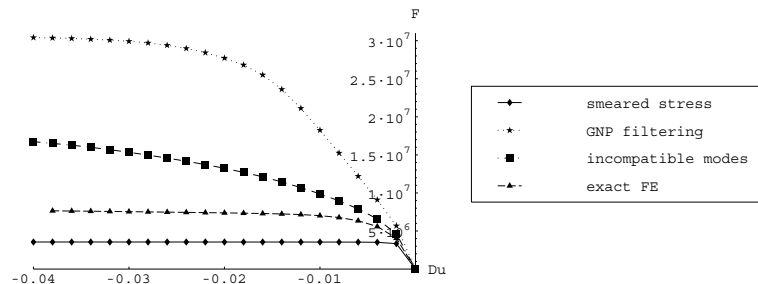


Fig. 16. Force–displacement diagrams obtained by different microstructure representations in the three-point bending test of the right half of the specimen shown in Fig. 15.

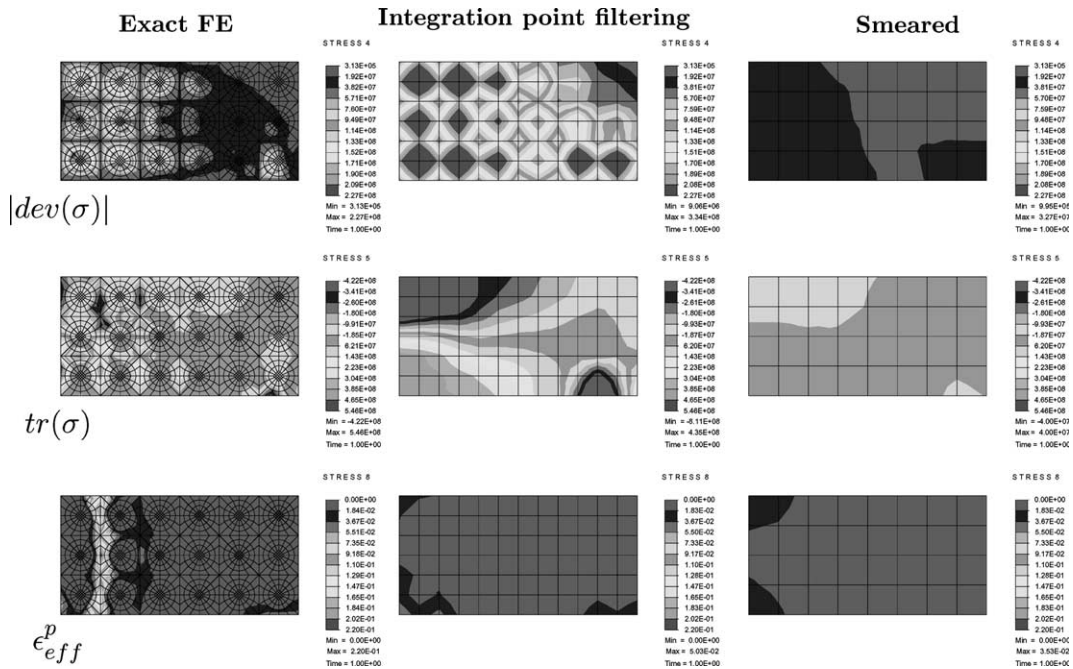


Fig. 17. Contour plots of deviatoric part, $|dev(\sigma)|$, spherical part, $tr(\sigma)$, of the stress tensor and the effective plastic deformation $\epsilon_{eff}^p = \int_0^t \sqrt{dev(\dot{\epsilon}^p)_{ij} dev(\dot{\epsilon}^p)_{ij}} dt$ for exact, integration point filtering and smeared representation.

In Fig. 17 we compare the stress fields for the three different microstructure representations. Like in the simple tension test, the GNP filtering and the smeared stress representations are not capable to reflect the localization of high stress values and possible fracture modes. In the contour (Fig. 17) of the effective plastic deformation obtained by the exact FE representation we note the localized shear band, which could not be detected by the GNP filtering and smeared stress microstructure representations.

5. Conclusions

In this work we have focused upon the class of problems of inelastic behavior of heterogeneous structures, which on one hand requires that one goes down to the microscale to more easily identify and describe the prominent dissipative mechanisms and, on the other hand, provides the constant communication between the scales. The proper order of strongly coupled iterative solutions at both scales is proposed, motivated by the operator split procedure for the classical plasticity.

The method proposed herein for dealing with multi-scale analysis of inelastic behavior of heterogeneous structures is very general in the sense that the finite element representation is employed at both scales, micro and macro. Therefore, a number of practical cases can easily be handled within the proposed framework.

As shown by this work, the method accuracy strongly depends on the level of the microstructure representation, where the exact finite element representation is proved to be the most accurate. However, it is the most costly in terms of finite element mesh preparation and the computational effort which is required. The efficiency of the method can be significantly improved if a convenient, structured microstructure representation is rendered more reliable. The incompatible mode structured mesh representation of the microstructure is shown to be the most suitable among the presented alternatives.

Acknowledgements

This work was supported by the French Ministry of Research (ACI “Jeunes Chercheurs”) and the Slovene Ministry of Education, Science and Sport.

References

- [1] M. Bornert, T. Bretheau, P. Gilormini, *Homogenization in Mechanics of Materials*, vol I&II, Hermes-Science, Paris, 2001 (in French).
- [2] P.P. Castaneda, P. Suquet, Non-linear composites, *Adv. Appl. Mech.* 34 (1998) 171–302.
- [3] A.J. Chorin, T.J.R. Hughes, M.F. McCracken, J.E. Marsden, Product formulas and numerical algorithms, *Commun. Pure Appl. Meth.* 31 (1978) 205–256.
- [4] J. Fish, O. Yu, Multiscale damage modelling for composite materials: theory and computational framework, *Int. J. Numer. Methods. Engrg.* 52 (2001) 151–191.
- [5] E.J. Garboczi, D.P. Bentz, The effect of statistical fluctuation, finite size error, and digital resolution on the phase percolation and transport property of the NIST cement hydration model, *Cement Concrete Res.* 31 (2001) 1501–1514.
- [6] S. Ghosh, K. Lee, P. Raghavan, A multi-level computational model for multi-scale damage analysis in composite and porous materials, *Int. J. Solids Struct.* 38 (2001) 2335–2385.
- [7] P. Gilormini, A shortcoming of the classical non-linear extension of the self-consistent model, *C.R. Acad. Sci. Paris*, t. 320 (116) (1995) 115–122.
- [8] A.L. Gurson, Continuum theory of ductile rupture by void nucleation and growth: Part I—Yield criteria and flow rules for porous ductile media, *J. Engrg. Mater. Technol.* 99 (1977) 1–15.
- [9] C. Huet, Application of variational concepts to size effects in elastic heterogeneous bodies, *J. Mech. Phys. Solids* 38 (1990) 813–841.
- [10] A. Ibrahimbegović, F. Gharzeddine, L. Chorfi, Classical plasticity and viscoplasticity models reformulated: theoretical and numerical implementation, *Int. J. Numer. Methods Engrg.* 42 (1999) 1499–1535.
- [11] A. Ibrahimbegović, D. Marković, F. Gatuingt, Constitutive model of coupled damage-plasticity and its finite element implementation, *Eur. J. Finite Elem.* 12 (4) (2003) 381–405.
- [12] A. Ibrahimbegović, D. Brancherie, Combined hardening and softening constitutive model of plasticity: precursor to shear slip line failure, *Comput. Mech.* 31 (2003) 88–100.
- [13] A. Ibrahimbegović, R.L. Taylor, On the role of invariance in geometrically exact structural theory at finite rotations, *Comput. Methods Appl. Mech. Engrg.* 191 (2002) 5159–5176.
- [14] A. Ibrahimbegović, E.L. Wilson, A modified method of incompatible modes, *Commun. Numer. Methods Engrg.* 8 (1991) 194203.
- [15] P. Ladevèze, O. Loiseau, D. Dureisseix, A micro–macro and parallel computational strategy for highly heterogeneous structures, *Int. J. Numer. Methods Engrg.* 52 (2001) 121–138.
- [16] J.L. Lions, *Asymptotic calculus of variations*, in *Singular perturbation and asymptotics*, Academic Press, New York, 1980.
- [17] H.G. Matthies, J. Steindorf, Strong coupling methods, in: *Proceedings Conference on Multifield Problems*, Stuttgart, Springer, Berlin, 2002.
- [18] C. Miehe, J. Schröder, J. Schotte, Computational homogenization analysis in finite plasticity: Simulation of texture development in polycrystalline materials, *Comput. Methods Appl. Mech. Engrg.* 171 (1999) 387–418.
- [19] H. Moulinec, P. Suquet, A numerical method for computing the overall response of non-linear composites with complex microstructure, *Comput. Methods Appl. Mech. Engrg.* 157 (1998) 69–94.
- [20] Q.S. Nguyen, B. Halphen, On generalized standard materials, *J. Mécanique (in French)* 13 (1975) 1–37.
- [21] J.T. Oden, K. Vemaganti, N. Moes, Hierarchical modeling of heterogeneous solids, *Comput. Methods Appl. Mech. Engrg.* 172 (1999) 3–25.
- [22] M. Ortiz, Y. Leroy, A. Needleman, A finite element method for localized failure analysis, *Comput. Methods Appl. Mech. Engrg.* 61 (1987) 189–214.
- [23] E. Sanchez-Palencia, *Non-homogeneous media and vibration theory*, in: *Lecture Notes in Physics*, vol. 127, Springer, Berlin, 1980.
- [24] J.C. Simo, T.J.R. Hughes, *Computational Inelasticity*, Springer, Berlin, 1998.
- [25] G.I. Taylor, Plastic strain in metals, *J. Inst. Met.* 62 (1938) 307–324.
- [26] V. Tvergaard, A. Needleman, Analysis of the cup-cone fracture in a round tensile bar, *Acta Metall. Mater.* 32 (1984) 157–169.
- [27] E.L. Wilson, The static condensation algorithm, *Int. J. Numer. Methods Engrg.* (1974).
- [28] P. Wriggers, T.I. Zohdi, Computational testing of new materials, in: *Proceedings ECCM 2001*, Crackow, Poland, 2001.
- [29] O.C. Zienkiewicz, R.L. Taylor, *The Finite Element Method*, vols. I–III, Butterworth Heineman, Oxford, 2000.